

## Article

# Investigation of the Microstructure and Wear Properties of Laser Clad Al-Si Coatings Containing Different Y<sub>2</sub>O<sub>3</sub> Contents

Dongdong Zhang <sup>1,2,3,\*</sup>, Xiya He <sup>3</sup>, Yali Gao <sup>3,\*</sup> and Baolong Qin <sup>3</sup>

<sup>1</sup> Key Laboratory of Bionic Engineering, Jilin University, Ministry of Education, Changchun 130025, China

<sup>2</sup> Gongqing Institute of Science and Technology, No. 1 Gongqing Road, Gongqing City 332020, China

<sup>3</sup> School of Mechanical Engineering, Northeast Electric Power University, No. 169 Changchun Road, Chuanying District, Jilin 132012, China

\* Correspondence: zhangdongdong@neepu.edu.cn (D.Z.); dehuigyl@126.com (Y.G.)

**Abstract:** Y<sub>2</sub>O<sub>3</sub>-reinforced Al-Si alloy coatings were prepared on the surface of a Mg alloy by the laser cladding technique. The microstructure, hardness, and wear resistance of the coatings were analyzed using an X-ray diffractometer, a scanning electron microscope, an energy spectrometer, a Vickers hardness tester, and a friction wear tester. The effect of different additions of Y<sub>2</sub>O<sub>3</sub> on the microstructure and properties of the coatings was investigated. The results indicate that the addition of Y<sub>2</sub>O<sub>3</sub> leads to a significant refinement of the grain size and a denser microstructure of the coatings. Coatings with a high Y<sub>2</sub>O<sub>3</sub> content provide superior hardness and wear resistance. With a Y<sub>2</sub>O<sub>3</sub> content of 7.5 wt.%, the coating exhibits the finest grain size, highest hardness, and smallest wear volume. Excessive amounts of Y<sub>2</sub>O<sub>3</sub>, however, cause a reduction in the surface properties of the coating.

**Keywords:** laser cladding; Y<sub>2</sub>O<sub>3</sub>; microstructure; wear resistance



**Citation:** Zhang, D.; He, X.; Gao, Y.; Qin, B. Investigation of the Microstructure and Wear Properties of Laser Clad Al-Si Coatings Containing Different Y<sub>2</sub>O<sub>3</sub> Contents. *Coatings* **2023**, *13*, 308. <https://doi.org/10.3390/coatings13020308>

Academic Editor: Angela De Bonis

Received: 25 December 2022

Revised: 23 January 2023

Accepted: 27 January 2023

Published: 30 January 2023



**Copyright:** © 2023 by the authors. Licensee MDPI, Basel, Switzerland. This article is an open access article distributed under the terms and conditions of the Creative Commons Attribution (CC BY) license (<https://creativecommons.org/licenses/by/4.0/>).

## 1. Introduction

Magnesium (Mg) alloys are composed of magnesium based on the addition of other elements, normally added elements such as Al, Zn, and Mn [1]. As one of the most widely used metallic materials in contemporary industry, Mg alloys are regarded as the green industrial materials of the 21st century [2,3]. The density of Mg alloy is low, only two-thirds that of Al, making it the lightest engineering material available [4]. Mg alloys have good heat dissipation, high specific strength, high specific stiffness, a high modulus of elasticity, good damping properties, and cutting properties [5]. It also exhibits excellent physical and chemical properties such as good biocompatibility, good recyclability, high hydrogen storage capacity, and a high theoretical specific capacity of the battery [6,7]. Owing to their excellent physical and chemical properties, Mg alloys are used in the aerospace, automotive, electronics, biomedical, and energy industries [8,9]. Nonetheless, the low hardness, poor wear resistance, and weak corrosion resistance of Mg alloys limit their further promotion [10–12].

For the improvement of the surface properties of Mg alloys, laser cladding technology is widely applied. Asghar et al. [13] successfully fabricated Ni60 coatings on LA43M Mg alloys by using the ultra-high-speed laser cladding technique and obtained superior surface mechanical properties. Sundaraselvan et al. [14] used laser melting technology to surface modify the AZ61 Mg alloy with nano-Al<sub>2</sub>O<sub>3</sub> and investigated the strengthening effect of nanoceramic particles. Studies have shown that laser cladding of alloy coatings can effectively address surface property defects in Mg alloys [15–18]. The binary alloys are often similar in composition to the matrix material, possess good physical and chemical compatibility with the matrix, and bond firmly after fusion coating [19–22]. Dziadoń et al. [23] investigated the microstructure of the surface layer of Mg laser alloyed with Al-Si. The differences in the microstructure of surface layers corresponded to the differences in their

wear resistance and corrosion resistance. Zhang et al. [24] prepared an Al-Si coating on the surface of a Mg-6Zn-1Ca alloy using laser cladding in order to improve the surface properties of Mg alloys. The results revealed that the coating mainly consisted of  $\alpha$ -Mg,  $\text{Mg}_2\text{Si}$  dendrites,  $\text{Mg}_{17}\text{Al}_{12}$ , and  $\text{Al}_3\text{Mg}_2$  phases. The microhardness of the coating (310 HV) was approximately five times higher than that of the substrate (54 HV). Wang [25] et al. designed three melting solutions by using pulsed direct current (P-DC) cold arc on the surface of AZ61 Mg alloy, namely Al-Si alloy ( $\text{AlSi}_5$ ), Al-Mn alloy ( $\text{AlMn}$ ), and Al-Mg alloy ( $\text{AlMg}_5$ ). The Al-Si alloy coating had the lowest wear rate, approximately 13.9% of that of the matrix. Laser cladding Al-Si alloy coatings significantly improves the surface properties of the Mg alloys. Additionally, the microstructure formed by adding  $\text{Y}_2\text{O}_3$  has pronounced effects on the friction and wear characteristics of the coating [26–28]. There is quite limited research into the improvement of Mg alloy surface coatings by means of  $\text{Y}_2\text{O}_3$ . Moreover, the relevant research mainly focuses on the improvement of coating performance by low rare earth oxide addition, and some research only takes it as one of the variables [29,30]. Therefore, studying the addition of rare earth oxides as the only variable and in the higher range is quite beneficial.

The AZ91 series of Mg alloys has the advantages of high yield, mature technology, and promising development. In this paper, the AZ91HP Mg alloy, which has better performance in the AZ91 series, was chosen as the substrate. The surface properties were improved by preparing Al-Si alloy coatings with  $\text{Y}_2\text{O}_3$  through laser cladding technology. The research focused on the effect of various  $\text{Y}_2\text{O}_3$  contents on the microstructure, Vickers hardness, and wear resistance of the cladding. The findings provide an experimental foundation and theoretical guidance for further improvement of the microstructure and wear properties of Mg alloys.

## 2. Materials and Methods

The cladding coating was prepared with Al-Si eutectic powder and  $\text{Y}_2\text{O}_3$  powder. The Al-Si eutectic powder has 99.9% purity, a particle size of 48–150  $\mu\text{m}$ , and a mass ratio of Al to Si of 88:12.  $\text{Y}_2\text{O}_3$  powder has a purity of 99.9% and an average particle size of 150  $\mu\text{m}$ . AZ91HP Mg alloy with dimensions of 30 mm  $\times$  15 mm  $\times$  10 mm was used as the substrate material, and the chemical compositions are shown in Table 1.

**Table 1.** AZ91HP component contents (wt.%).

Element	Al	Zn	Mn	Si	Fe	Cu	Ni	Be	Mg
content	8.8900	0.5620	0.2041	0.0443	0.0030	0.0034	0.0090	0.0012	balance

The composite coating was prepared using a transverse flow  $\text{CO}_2$  laser processing system (DL-HL-T2000). The specific experimental parameters are shown in Table 2. The experiments were carried out with a spot diameter of 3 mm for laser cladding, a prefabricated coating thickness of 1 mm, a coating lap rate of 30%, and argon as a protective gas with a flow rate of 5 L/min.

**Table 2.** Experimental parameters for laser cladding coatings.

Order	Al-Si (wt.%)	$\text{Y}_2\text{O}_3$ (wt.%)	Power (W)	Scanning Speed (mm/min)
1	100	0	1300	400
2	97.5	2.5	1300	400
3	95	5	1300	400
4	92.5	7.5	1300	400
5	90	10	1300	400

A specimen block of size 12 mm  $\times$  12 mm  $\times$  10 mm was obtained by wire cutting, and the specimen was ground and polished with a polishing machine. An X-ray diffraction

analyzer (TD-3500X) was used to analyze the phase of the laser cladded specimen surface. The specimens were subjected to an etching treatment using a solution of 10 mL HF and 15 mL HCl mixed with 90 mL of H<sub>2</sub>O. The specimens were corroded for 2 s and then cleaned off the surface with ethylene glycol. The scanning electron microscope (JSM-7610s) was used for the microstructure tests. The equipment was used to observe the microstructure of specimen cross-sections and wear surfaces and to measure the chemical element distribution in the coating using its accompanying energy dispersive spectroscopy (EDS).

The hardness gradient performance of the cross-section of the laser cladding samples was tested by the Vickers hardness tester (HXD-1000TMC/LCD). The experimental load was 5 g, and the load retention time was 10 s. One data point was measured every 0.05 mm, taking the average of three parallel points as the hardness value. The wear resistance of the specimens was tested using a high-speed reciprocating fatigue friction and abrasion tester (MGW-02). The specimens were tested for 20 min at a test force of 3 N and a frequency of 10 Hz. The pair of grinding balls used were GCr15 steel, and the reciprocal wear distance was 3 cm. The width of the wear traces was measured using scanning electron microscopy to calculate the wear volume. The calculation equation is as follows:

$$\theta = 2 \times \arcsin\left(\frac{L_c}{2R}\right), \quad (1)$$

$$V = S \times L = \left(\frac{\theta \times R^2}{2} - \frac{\sin\theta \times R^2}{2}\right) \times L, \quad (2)$$

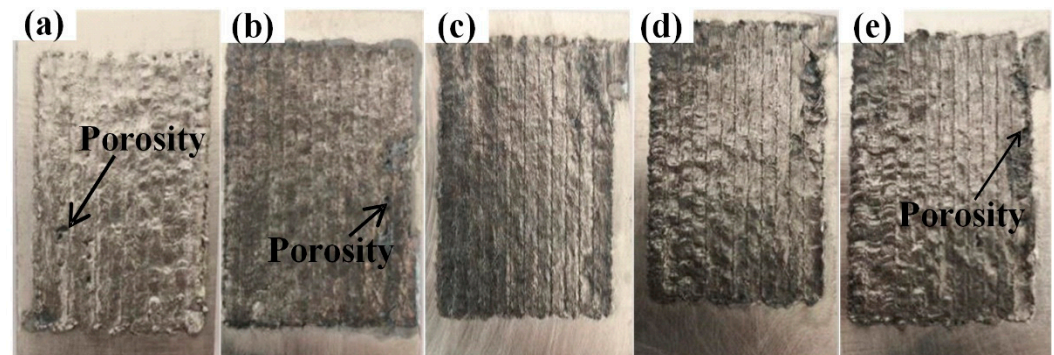
where,  $\theta$  is the center angle corresponding to the wear trace,  $L_c$  is the width of the wear trace,  $R$  is the radius of the grinding ball,  $L$  is the length of the wear trace (total reciprocating distance), and  $S$  is the area of the wear trace profile.

### 3. Results and Discussion

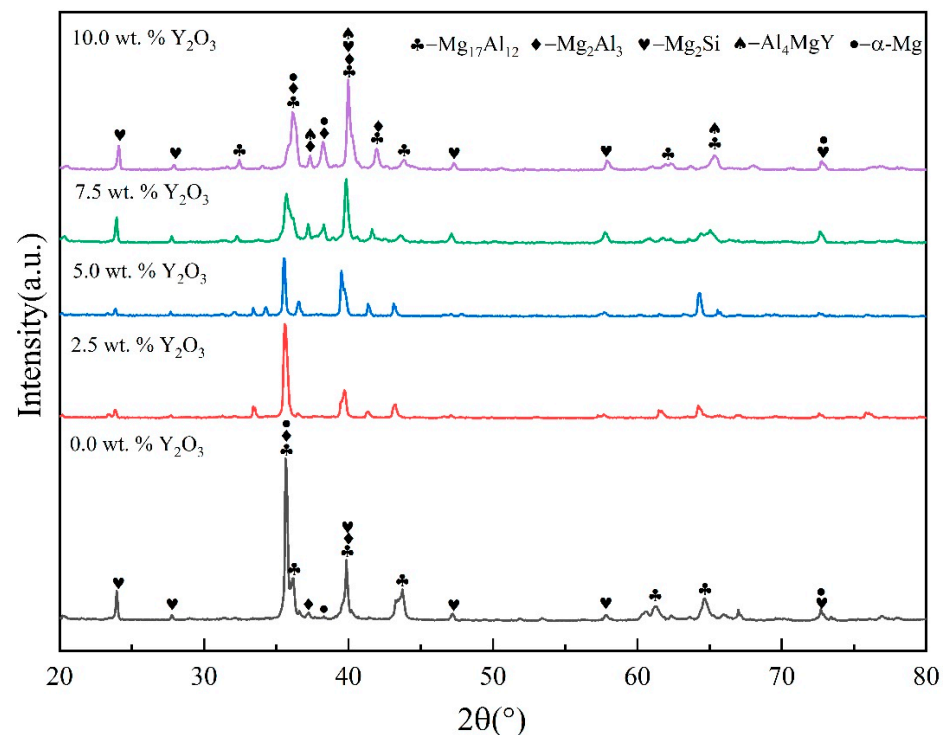
Figure 1 shows the macroscopic surface morphology of the coatings with various Y<sub>2</sub>O<sub>3</sub> contents. As seen in Figure 1, the coatings exhibit a metallic lustre. The surface of the five specimens shows no oxidation blackening, which indicates that the protective gas flow rate was controlled within a reasonable range. The relatively flatter coating can be clearly observed in Figure 1b–e. This indicates that the addition of Y<sub>2</sub>O<sub>3</sub> increases the absorption of the laser, which results in a more uniform heating of the coating. Some porosities can be observed in Figure 1a,b,e. The poor fluidity of the melt pool leads to the formation of cavities, whereas the addition of Y<sub>2</sub>O<sub>3</sub> can significantly improve the fluidity of the melt pool [29–31]. The coatings in Figure 1a,b have poor melt pool fluidity caused by the absence of Y<sub>2</sub>O<sub>3</sub> or low Y<sub>2</sub>O<sub>3</sub> content, resulting in the appearance of porosities. The coatings in Figure 1c,d have no porosity owing to the moderate addition of Y<sub>2</sub>O<sub>3</sub>, which improves the fluidity of the coating and allows the gases generated during the laser cladding process to escape before the melt pool solidifies. While some porosities are generated again in Figure 1e caused by the addition of excessive amounts of Y<sub>2</sub>O<sub>3</sub>, resulting in the blocking of the melt pool flow and impeding the discharge of gas.

Figure 2 presents the XRD results of the laser cladding coatings with various Y<sub>2</sub>O<sub>3</sub> contents. As shown, the coatings containing Y<sub>2</sub>O<sub>3</sub> mainly consist of Mg<sub>17</sub>Al<sub>12</sub>, Mg<sub>2</sub>Al<sub>3</sub>, Mg<sub>2</sub>Si, Al<sub>4</sub>MgY, and  $\alpha$ -Mg, while the Al<sub>4</sub>MgY phase is absent in coatings without Y<sub>2</sub>O<sub>3</sub> addition. The original phases in the AZ91HP Mg alloy are Mg<sub>17</sub>Al<sub>12</sub> and  $\alpha$ -Mg. Due to the effect of the high-energy laser beam, the Mg alloy fully reacts with the coating material to produce a variety of intermetallic compounds as well as Al<sub>4</sub>MgY rare earth compounds. The diffraction peaks of the coating are concentrated between 35° and 40° with the high peaks being all Mg-containing phases, indicating that Mg diffuses into the coating through the melt pool and reacts fully with the coating elements to produce a variety of phase structures. Furthermore, the addition of Y<sub>2</sub>O<sub>3</sub> resulted in a significant alteration in the phase diffraction intensity of the coating, as shown by the fact that a high peak at 36° appears in the coating without Y<sub>2</sub>O<sub>3</sub>, while a trend of decreasing and then increasing a peak

at  $36^\circ$  occurs with increasing  $Y_2O_3$  content. Similarly, a peak of  $39^\circ$  occurs in the coating without  $Y_2O_3$ , while the peak shows an increasing trend as the  $Y_2O_3$  content increases from 2.5 to 10.0 wt.%.



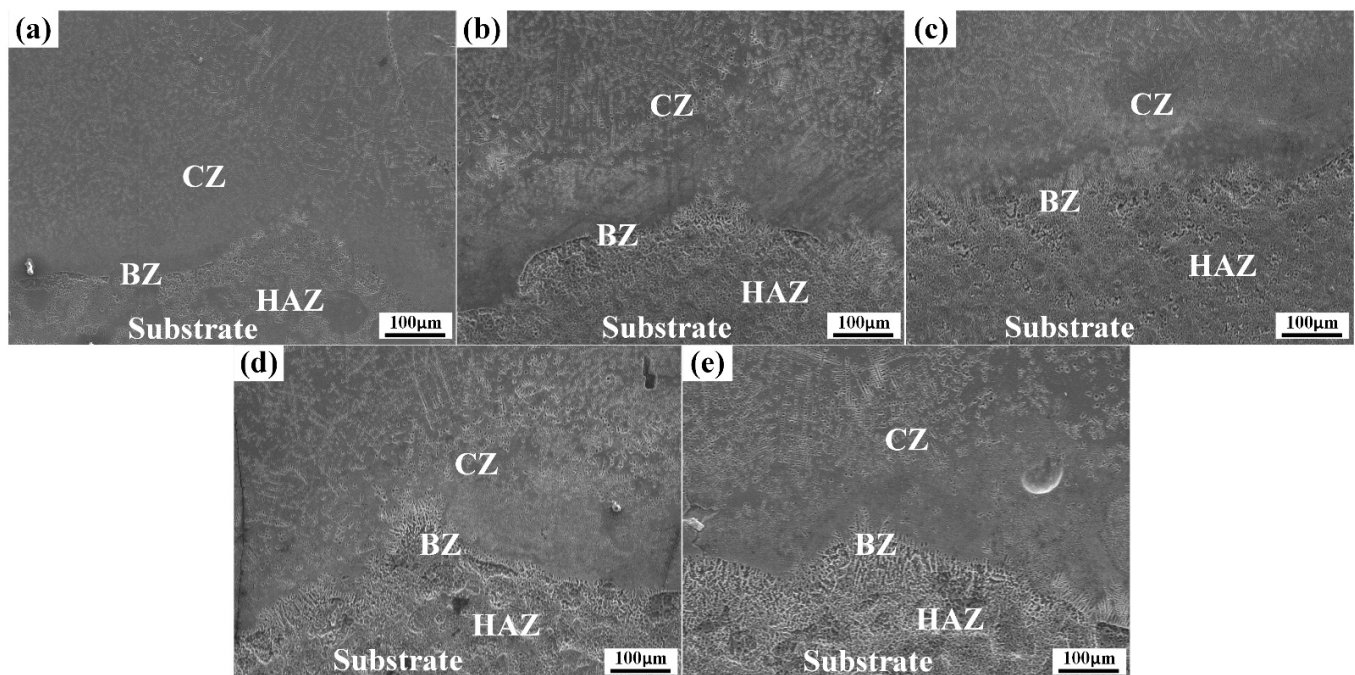
**Figure 1.** Surface morphology of coatings with various  $Y_2O_3$  contents (a) 0 wt.%; (b) 2.5 wt.%; (c) 5 wt.%; (d) 7.5 wt.%; (e) 10 wt.%.



**Figure 2.** XRD results of coatings with various  $Y_2O_3$  contents.

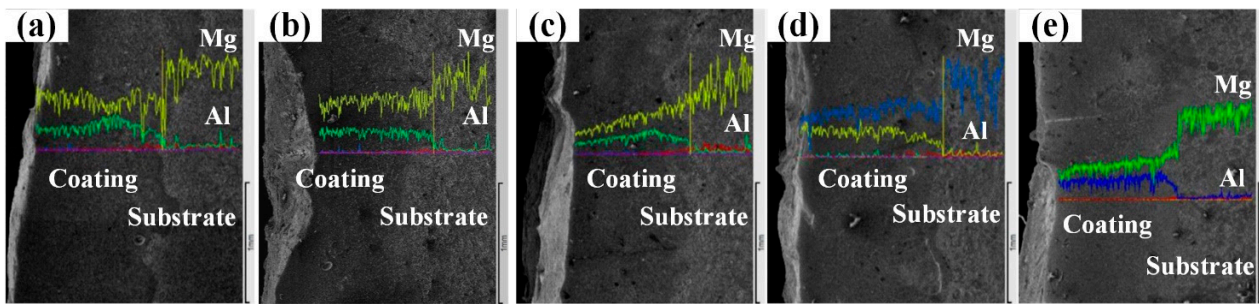
Figure 3 illustrates the cross-sectional microstructure of the coating with various  $Y_2O_3$  contents. The coating consists of four parts, from top to bottom: the cladding zone (CZ), the bonding zone (BZ), the heat-affected zone (HAZ), and the substrate. The strip between the coating and the substrate is wavy. The reason for this is that the different melting points of the native  $\alpha$ -Mg in the Mg alloy and the dissociated eutectic tissue at the grain boundaries, leads to a different amount of melting at different locations on the surface of the substrate. Thus, the surface of the substrate appears as a local melting depression area, which makes the solidified substrate and coating bonding interface wavy. This further confirms that the coating shows a good metallurgical bond with the substrate.





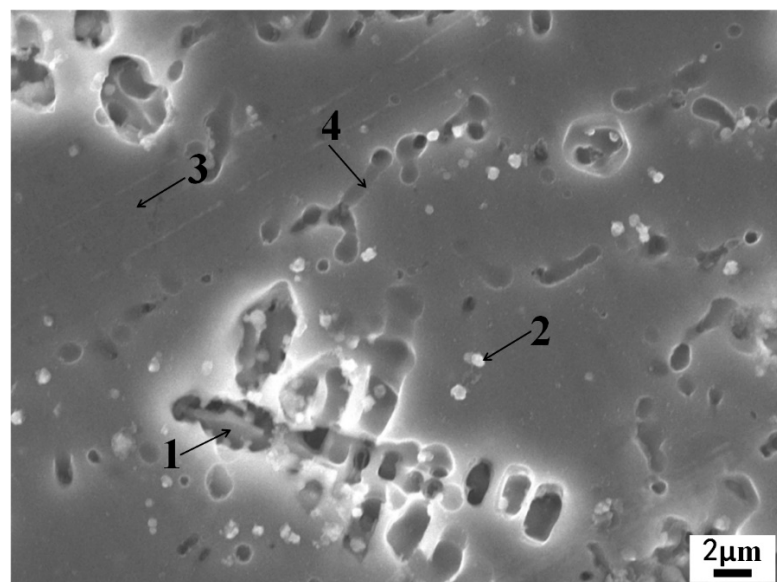
**Figure 3.** Cross-sectional microstructure of coatings with various  $Y_2O_3$  contents (a) 0 wt.%; (b) 2.5 wt.%; (c) 5 wt.%; (d) 7.5 wt.%; (e) 10 wt.%.

Figure 4 shows the results of the line scan of the coating cross-sections with various  $Y_2O_3$  contents. Using the internal direction of the coating as the positive horizontal axis and the elemental content as the vertical axis, it can be seen that the elemental content of Mg gradually increases and rises steeply at the interface between the substrate and the coating, reaching a maximum in the substrate, while the elemental content of Al shows a decreasing trend, reaching a minimum in the substrate. The most abundant element in the coating is Mg, which reveals that the substrate surface layer melts instantly under the action of the laser to form a molten pool. It is conducive to a good bond between the coating material and the substrate, but this also results in the problem of an excessive dilution rate. From Figure 4a–d, the Mg element content in the coating gradually decreases as the  $Y_2O_3$  content increases until the  $Y_2O_3$  content is 7.5 wt.%, at which point the minimum amount of elemental Mg is reached and the lowest dilution rate is achieved. This is because  $Y_2O_3$  has a very high melting point. Incorporating it into the coating increases the latent heat of melting the alloy powder, lowers the liquid phase temperature in the melt pool, raises the solid phase temperature, and reduces the time for solidification, which allows less time for the elements to diffuse [32,33]. This allows more of the coating elements to remain in the melt pool and inhibits the massive influx of Mg elements into the coating, thus enhancing the surface properties. In addition, the high melting point  $Y_2O_3$  does not melt rapidly at the first stage of melt pool formation; instead, it is dispersed in different parts of the melt pool to absorb energy, slowing down the increase in melt pool temperature, reducing the movement of Mg atoms, and slowing down element diffusion. As the  $Y_2O_3$  content continues to increase, the Mg element content in the coating begins to rise, as shown in Figure 4e, indicating that the addition of excessive  $Y_2O_3$  will increase the dilution rate of the coating. This is attributed to the presence of the higher melting point  $Y_2O_3$  in the melt pool over a large area, which impedes the convection between the Mg alloy and the Al-Si alloy in the molten state and reduces the convective heat exchange efficiency in the melt pool. This prolongs the existence of the melt pool and increases the opportunity for chemical element diffusion, which allows a large number of Mg atoms to enter the coating and the dilution rate to rise. The Mg content of the coatings with  $Y_2O_3$  is lower than that of the coatings without  $Y_2O_3$ , which means that the addition of  $Y_2O_3$  in the right amount can reduce the dilution rate of the coatings.



**Figure 4.** Cross-sectional line scan results of coatings with various  $Y_2O_3$  contents (a) 0 wt.%; (b) 2.5 wt.%; (c) 5 wt.%; (d) 7.5 wt.%; (e) 10 wt.%.

Figure 5 shows the microstructure of the coating with a  $Y_2O_3$  content of 2.5 wt.%. The coating consists mainly of dendritic crystals (1), a punctate phase (2), a matrix phase (3), and an acicular phase (4). Dendrites are generated because the grains within the coating are rough interfacial structures at the time of crystallization and the temperature gradient is negative, with a large but unstable supercooling at the front of the solid-liquid interface. The crystallization proceeds in that direction when the supercooling at the rest of the interface spikes, thus making it more favorable for the tip to grow in that direction. The tip also grows laterally, but not as fast as the front of the tip due to the latent heat of crystallization, resulting in the tip growing rapidly into elongated grains called primary dendrites. The secondary dendrites are those that grow in other directions due to fluctuations in the surrounding supercooling. The latent heat of crystallization causes the subcooling to decrease below a critical level, so the free energy generated during crystallization is lower than the surface free energy, allowing secondary dendrites to not continue to grow and form dendrite-like grains.



**Figure 5.** Microstructure of the 2.5 wt.%  $Y_2O_3$  coating.

The point scan of the points in Figure 5 using EDS gave the chemical element composition as shown in Table 3. The ratio of Mg atoms to Si atoms at point 1 is approximately 2:1, which is close to the atomic ratio of the  $Mg_2Si$  phase, so the phase is judged to be the  $Mg_2Si$  hard phase. The ratio of Al, Mg, and Y atoms at point 2 is approximately 4:1:1, so this is the  $Al_4MgY$  phase. The ratio of Mg atoms to Al atoms at point 3 is approximately 3:2, which is close to the atomic ratio of  $Mg_{17}Al_{12}$ , indicating that this phase is  $Mg_{17}Al_{12}$ . The ratio of Mg atoms to Al atoms at point 4 is approximately 2:3, indicating that this phase is  $Mg_2Al_3$ .

**Table 3.** Point scan results for coatings containing 2.5 wt.%  $Y_2O_3$ .

Order	Mg (at.%)	Al (at.%)	Si (at.%)	O (at.%)	Y (at.%)
1	66.17	2.09	30.12	0.80	0.82
2	16.89	65.48	0.92	0.61	16.10
3	59.88	39.73	0.12	0.27	0.00
4	39.53	58.25	0.27	1.90	0.05

Figure 6 illustrates the evolution of the microstructure for the 2.5 wt.%  $Y_2O_3$  coating at different depths. A clear change in grain morphology from the top to the bottom of the coating can be observed. Figure 6a reveals the top of the coating, where the grains are relatively sparse but fine. This is because the surface layer is exposed to direct laser light, resulting in the burnout of some elements, so there is a relatively loose microstructure. There are many channels for heat dissipation from the top of the coating, which means that free energy drops more quickly in the upper part of the melt pool, making the conversion of the surface liquid phase into a solid phase more dynamic. The rapid drop in temperature causes the top layer to have a lower actual crystallization temperature, resulting in a larger degree of subcooling. This leads to a refinement of the grain size, so the top layer has finer grains. Figure 6b shows the microstructure of the upper-middle part of the coating. The microstructure is much denser and has the finest grain size, exhibiting the best overall coating quality. There is no significant elemental burning as in the surface layer, and some of the slag and impurities from the laser coating float up to this area, which provides nuclei for crystallization and thus increases the nucleation rate to refine the grains. Figure 6c shows the lower-middle of the coating. The grains in Figure 6c are significantly coarser than in the upper part. This is because the microstructure has limited heat dissipation channels during crystallization, and there is a loss of laser energy density transfer resulting in a low melt pool temperature, which reduces subcooling and coarsens the grains. Figure 6d depicts the bottom of the coating. The microstructure in this area has the coarsest grains. This area has the worst heat dissipation and is affected by the latent heat of crystallization in the upper layers, which causes poor fluidity and low nucleation rates, producing grains that are coarse.

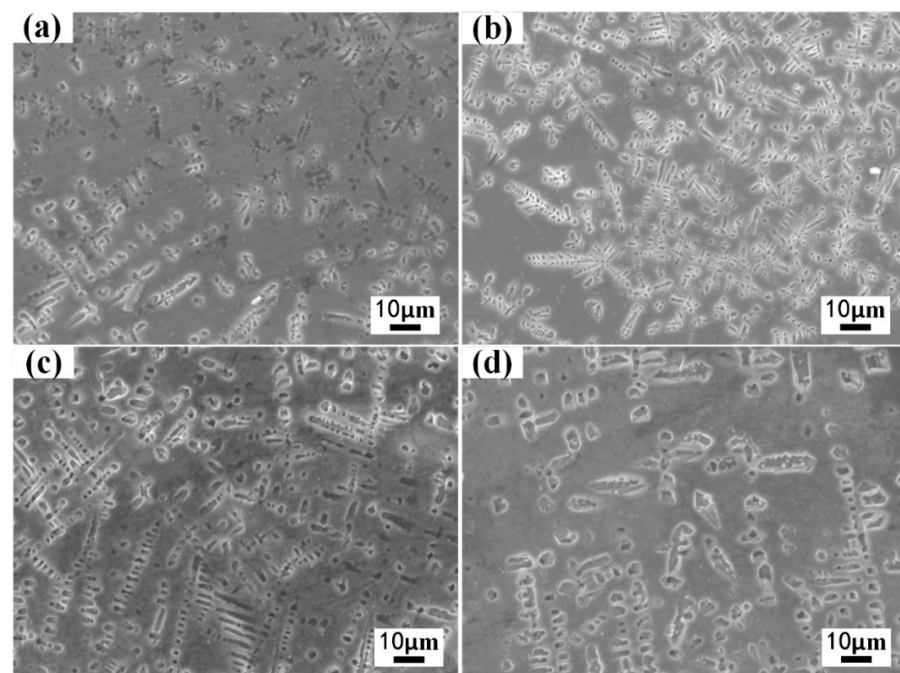
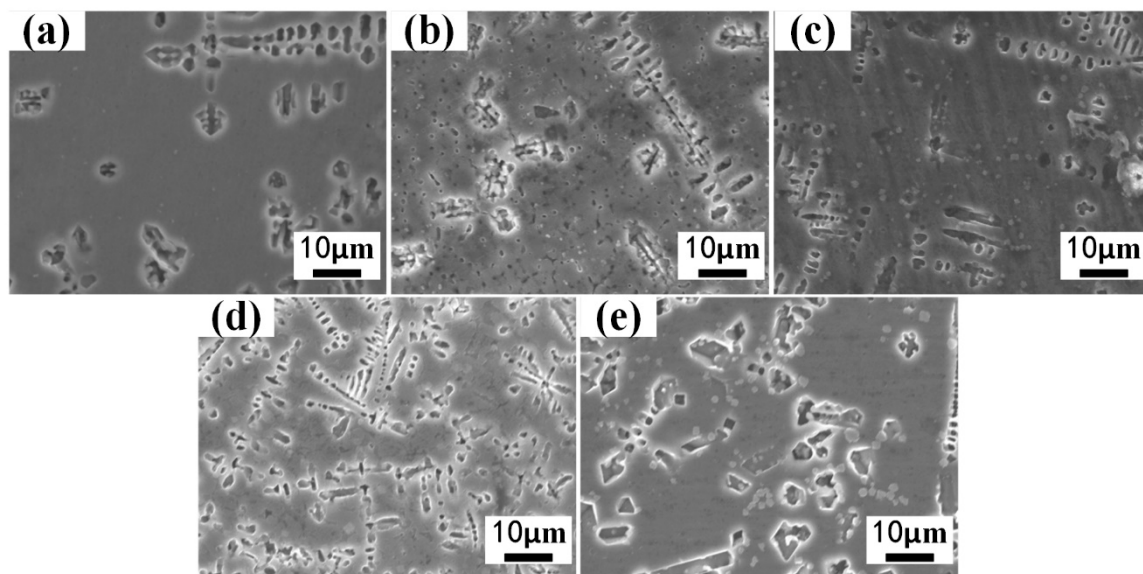
**Figure 6.** Microstructure of the coating with 2.5 wt.%  $Y_2O_3$  at different depths: (a) top; (b) upper middle; (c) lower middle; and (d) bottom.



Figure 7 illustrates the microstructure of the coatings with different  $Y_2O_3$  contents. As shown, the coating without  $Y_2O_3$  has the coarsest grains, while the coating microstructure is significantly refined after the addition of  $Y_2O_3$ . The coating microstructure gradually becomes finer with the increase of  $Y_2O_3$  content in a certain range, and the coating microstructure is finest when the content of  $Y_2O_3$  is 7.5 wt.%. This is attributed to the denser  $Y_2O_3$ , which tends to enrich at the front end of the solid-liquid interface, thus increasing the component subcooling of the coating. As the  $Y_2O_3$  content increases, the subcooling is greater, which refines the grain size. Additionally, the increased  $Y_2O_3$  content improves the absorption rate of the coating material by the laser, which makes the coating more uniformly heated, resulting in a denser and more homogeneous microstructure. The addition of  $Y_2O_3$  also increases the nucleation rate during melt pool crystallization. The high melting point of  $Y_2O_3$  acts as a heterogeneous impurity, offering ready-made nuclei for crystallization, which increases the number of nuclei and thus refines the microstructure [27]. When the  $Y_2O_3$  content exceeds 7.5 wt.%, the grain coating becomes coarser, but it still outperforms the coating without  $Y_2O_3$ , as shown in Figure 7e. This is because the excess  $Y_2O_3$  is difficult to melt in the melt pool, which impedes convective heat exchange in the melt pool and reduces the degree of subcooling during crystallization, resulting in a reduction in grain refinement. Moreover, when  $Y_2O_3$  acts as a heterogeneous mass to provide nucleation, excessive content results in its massive enrichment. This reduces the available nucleation substrate, and heterogeneous nucleation ceases once the nucleation substrate is completely encapsulated by the crystal nucleus, resulting in a decrease in the nucleation rate and a reduction in the number of grains.



**Figure 7.** Microstructure of coatings with various  $Y_2O_3$  contents (a) 0 wt.%; (b) 2.5 wt.%; (c) 5 wt.%; (d) 7.5 wt.%; (e) 10 wt.%.

The hardness curves of the coatings with different  $Y_2O_3$  contents are presented in Figure 8. The curves are roughly divided into three parts: the surface of the melt layer; the melt zone; the heat-affected zone. The hardness of the coatings prepared by laser cladding technology (226.3–285.0 HV) is much higher than that of the substrate (80.0 HV). This is owing to the presence of phases such as  $Mg_2Si$ ,  $Mg_2Al_3$ , and  $Al_4MgY$  in the coating, which have a finer grain structure, a higher hardness, and are distributed in various parts of the coating, impeding dislocation movement and greatly enhancing the hardness of the coating. The coating also exhibits a significant refinement of the microstructure, which leads to a fine crystal strengthening effect, resulting in a much higher hardness than the substrate. The hardness of each coating follows a trend of increasing, then leveling off, and finally decreasing to the substrate hardness, with the maximum hardness occurring in the melt



zone of the coating. This is because the direct irradiation of the laser causes burnout of the most superficial elements, which results in a thinning of the surface microstructure and a reduction in hardness. With the increase in  $Y_2O_3$  content, the average hardness of each coating in order is 226.3 HV, 266.0 HV, 273.8 HV, 285.0 HV, and 234.8 HV. The hardness of the coating is seen to increase and then decrease as the content of  $Y_2O_3$  increases, reaching a maximum value (285.0 HV) at 7.5 wt.%  $Y_2O_3$ . The addition of  $Y_2O_3$  increases the subcooling of the crystals, which improves the nucleation rate and limits the growth of the grains, thus increasing the degree of grain refinement with increasing content. Furthermore, the decomposition of  $Y_2O_3$  in the melt pool produces rare earth compounds. The compounds possess the effect of purifying the melt pool, which results in a denser and more homogeneous melt pool, increasing the hardness. The average hardness of the coating starts to decrease as the  $Y_2O_3$  content continues to increase but remains higher than the average hardness of the coating without the  $Y_2O_3$ . An excessive amount of  $Y_2O_3$  (over 7.5 wt.%) increases the overall melting point of the coating, decreases the subcooling, and reduces the nucleation rate, causing coarsening of the grains and a decrease in hardness.

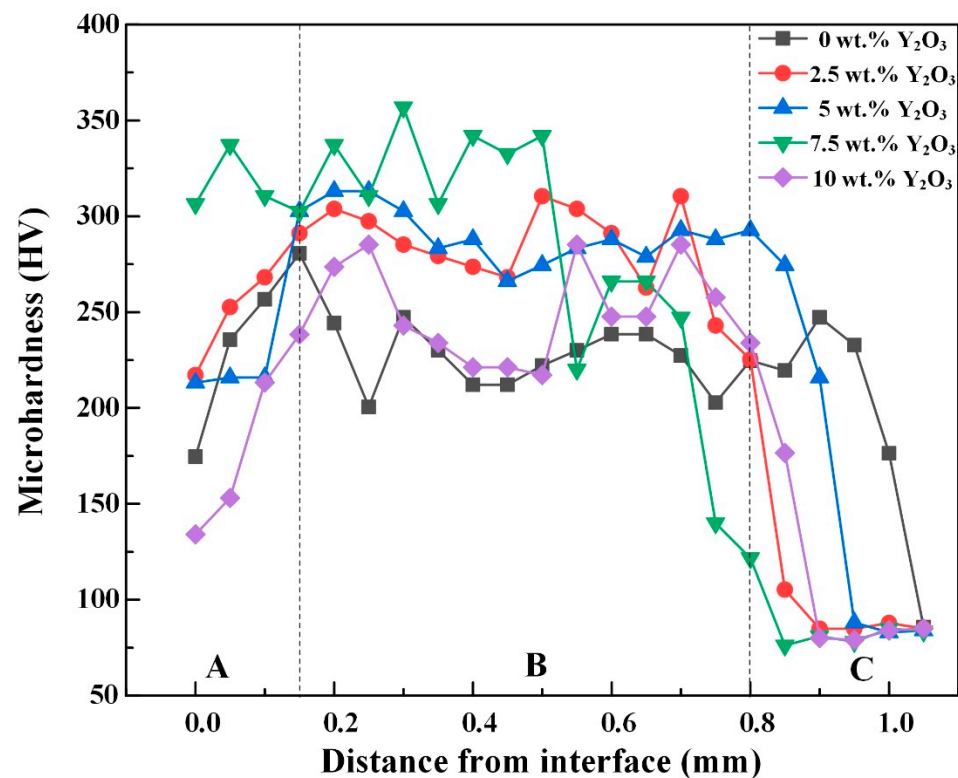


**Figure 8.** Hardness of coatings with various  $Y_2O_3$  contents: A: the surface of the melt layer; B: the melt zone; C: the heat-affected zone.

The wear volume of the coating with various  $Y_2O_3$  contents is presented in Figure 9. As shown, the wear volume of the coating is significantly lower than that of the substrate. The presence of the hard phase in the coating changes the contact between the coating and the grinding ball, decreasing the contact area and reducing the tendency to adhere. The coating microstructure is significantly refined, which strengthens the coating properties and increases the hardness and wear resistance of the coating. The wear resistance was further improved by the addition of  $Y_2O_3$  to the coating. As the  $Y_2O_3$  content increases, the wear volume of the coating first decreases and then increases, but both are smaller than the wear volume of the substrate. The minimum value ( $0.4584 \text{ mm}^3$ ) is reached when the  $Y_2O_3$  content is 7.5 wt.%, which is only 26.68% of the wear volume of the substrate. The addition of  $Y_2O_3$  refines the grain size and makes the coating more evenly distributed, increasing the surface hardness and enhancing wear resistance. With the continued increase in  $Y_2O_3$

content, however, the wear volume of the coating with a  $\text{Y}_2\text{O}_3$  content of 10 wt.% increases compared to the wear volume of the coating at 7 wt.%. Excess  $\text{Y}_2\text{O}_3$  reduces the fluidity of the melt pool, hinders the heat dissipation of the melt pool, and decreases the degree of subcooling, resulting in larger grains and an uneven microstructure distribution. This microstructure presents lower surface coating hardness and poorer wear resistance.

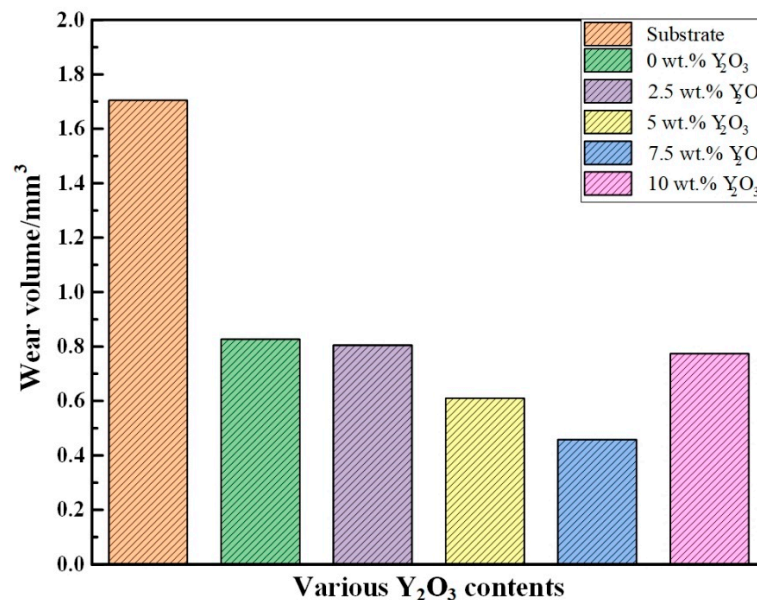


**Figure 9.** Wear volume of coatings with various  $\text{Y}_2\text{O}_3$  contents.

Figure 10 shows the wear morphology of the 10 wt.%  $\text{Y}_2\text{O}_3$  coating. Clear furrows can be seen in Figure 10a, and the partial enlargement of the wear morphology is given in Figure 10b. From Figure 10, one can observe clear signs of spalling. The coating suffered from abrasive and adhesive wear during the experiment. There is the relative movement between the grinding ball and the hard phase exposed to the coating surface by friction, which results in abrasive wear. This form of wear causes a large number of furrows on the wear surface. In addition, the reciprocating motion of the friction test generates heat that softens the coating, which causes bonding at the point of contact between the coating and the grinding ball. This results in adhesive wear, which causes extensive spalling of the wear surface.

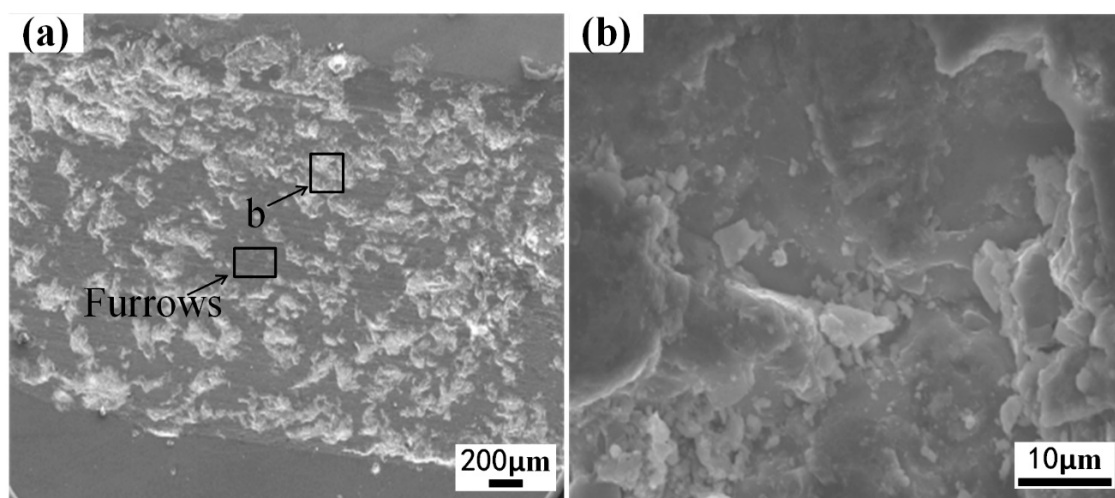


**Figure 10.** Wear morphology of the coating containing 10 wt.%  $\text{Y}_2\text{O}_3$ : (a) Surface wear morphology; (b) Local magnified of wear morphology.

#### 4. Conclusions

The microstructural evolution, Vickers hardness, and friction wear properties of the clad coatings with different  $Y_2O_3$  contents were investigated. The addition of  $Y_2O_3$  improves the surface morphology of the coating and refines the coating grains, thus achieving a significant improvement in the surface properties of the coating. As the  $Y_2O_3$  content increases, the coating grains gradually become finer and then coarser, and the surface hardness and wear resistance also first strengthen and then weaken. The coating with 7.5 wt.%  $Y_2O_3$  exhibits the finest grains, the highest density, and the best surface properties, with an average hardness of (285.0 HV), 3.6 times that of the substrate, and a wear volume of (0.4584 mm<sup>3</sup>), 26.68% that of the substrate. Coatings with a high  $Y_2O_3$  content have greater hardness and a higher wear resistance within a certain range of additions. Excess  $Y_2O_3$  causes a reduction in the surface properties of the coating.

**Author Contributions:** Conceptualization, D.Z. and Y.G.; methodology, D.Z. and Y.G.; validation, B.Q.; formal analysis, X.H.; investigation, B.Q.; resources, D.Z. and Y.G.; writing—original draft preparation, D.Z. and X.H.; writing—review and editing, X.H.; supervision, D.Z. and Y.G.; funding acquisition, D.Z. and Y.G. All authors have read and agreed to the published version of the manuscript.

**Funding:** This research was funded by the Science and Technology Project of the Jilin Provincial Education Department, grant number JJKH20220098KJ.

**Institutional Review Board Statement:** Not applicable.

**Informed Consent Statement:** Not applicable.

**Data Availability Statement:** Data is only available upon request due to restrictions such as privacy or ethical considerations. The data presented in this study are available on request from the corresponding author.

**Acknowledgments:** This thesis work is supported by Northeastern Electric Power University.

**Conflicts of Interest:** The authors declare no conflict of interest.

#### References

- Jayasathyakawin, S.; Ravichandran, M.; Baskar, N.; Chairman, C.A.; Balasundaram, R. Mechanical Properties and Applications of Magnesium Alloy—Review. *Mater. Today Proc.* **2020**, *27*, 909–913. [\[CrossRef\]](#)
- Song, J.; She, J.; Chen, D.; Pan, F. Latest Research Advances on Magnesium and Magnesium Alloys Worldwide. *J. Magnes. Alloy.* **2020**, *8*, 1–41. [\[CrossRef\]](#)
- You, S.; Huang, Y.; Kainer, K.U.; Hort, N. Recent Research and Developments on Wrought Magnesium Alloys. *J. Magnes. Alloy.* **2017**, *5*, 239–253. [\[CrossRef\]](#)
- Makwana, D.; Bhingole, P.P. Electrochemical and Plasma Surface Modification of Magnesium and Its Alloy: Review. *Mater. Today Proc.* **2018**, *5*, 18260–18267. [\[CrossRef\]](#)
- Wang, X.J.; Xu, D.K.; Wu, R.Z.; Chen, X.B.; Peng, Q.M.; Jin, L.; Xin, Y.C.; Zhang, Z.Q.; Liu, Y.; Chen, X.H.; et al. What Is Going on in Magnesium Alloys? *J. Mater. Sci. Technol.* **2018**, *34*, 245–247. [\[CrossRef\]](#)
- Pan, F.; Yang, M.; Chen, X. A Review on Casting Magnesium Alloys: Modification of Commercial Alloys and Development of New Alloys. *J. Mater. Sci. Technol.* **2016**, *32*, 1211–1221. [\[CrossRef\]](#)
- Chen, J.; Tan, L.; Yu, X.; Etim, I.P.; Ibrahim, M.; Yang, K. Mechanical Properties of Magnesium Alloys for Medical Application: A Review. *J. Mech. Behav. Biomed. Mater.* **2018**, *87*, 68–79. [\[CrossRef\]](#)
- Yeganeh, M.; Mohammadi, N. Superhydrophobic Surface of Mg Alloys: A Review. *J. Magnes. Alloy.* **2018**, *6*, 59–70. [\[CrossRef\]](#)
- Joost, W.J.; Krajewski, P.E. Towards Magnesium Alloys for High-Volume Automotive Applications. *Scr. Mater.* **2017**, *128*, 107–112. [\[CrossRef\]](#)
- Zhang, H.; Wang, S.; Yang, X.; Hao, S.; Chen, Y.; Li, H.; Pan, D. Interfacial Characteristic and Microstructure of Fe-Based Amorphous Coating on Magnesium Alloy. *Surf. Coatings Technol.* **2021**, *425*, 127659. [\[CrossRef\]](#)
- de Oliveira, L.A.; da Silva, R.M.P.; Rodas, A.C.D.; Souto, R.M.; Antunes, R.A. Surface Chemistry, Film Morphology, Local Electrochemical Behavior and Cytotoxic Response of Anodized AZ31B Magnesium Alloy. *J. Mater. Res. Technol.* **2020**, *9*, 14754–14770. [\[CrossRef\]](#)
- Hu, L.; Meng, Q.; Chen, S.; Wang, H. Effect of Zn Content on the Chemical Conversion Treatments of AZ91D Magnesium Alloy. *Appl. Surf. Sci.* **2012**, *259*, 816–823. [\[CrossRef\]](#)
- Asghar, O.; Li-Yan, L.; Yasir, M.; Chang-Jiu, L.; Cheng-Xin, L. Enhanced Tribological Properties of LA43M Magnesium Alloy by Ni60 Coating via Ultra-High-Speed Laser Cladding. *Coatings* **2020**, *10*, 638. [\[CrossRef\]](#)



14. Sundaraselvan, S.; Senthilkumar, N. Surface modification of AZ61 magnesium alloy with nano-Al<sub>2</sub>O<sub>3</sub> using laser cladding technique: Optimisation of wear properties through hybrid GRA-PCA. *Int. J. Rapid Manuf.* **2019**, *8*, 221. [\[CrossRef\]](#)
15. Zhu, Q.; Liu, Y.; Zhang, C. Laser Cladding of CoCrFeNi High-Entropy Alloy Coatings: Compositional Homogeneity towards Improved Corrosion Resistance. *Mater. Lett.* **2022**, *318*, 132133. [\[CrossRef\]](#)
16. Lu, H.; Li, W.; Qin, E.; Liu, C.; Liu, S.; Zhang, W.; Wu, S. The Gradient Microstructure and High-Temperature Wear Behavior of the CoCrMoSi Coating by Laser Cladding. *J. Therm. Spray Technol.* **2021**, *30*, 968–976. [\[CrossRef\]](#)
17. Gu, Z.; Mao, P.; Gou, Y.; Chao, Y.; Xi, S. Microstructure and Properties of MgMoNbFeTi<sub>2</sub>Y<sub>x</sub> High Entropy Alloy Coatings by Laser Cladding. *Surf. Coatings Technol.* **2020**, *402*, 126303. [\[CrossRef\]](#)
18. Meng, G.H.; Protasova, N.A.; Kruglov, E.P.; Lin, X.; Xie, H.; Ding, X. Solidification Behavior and Morphological Evolution in Laser Surface Forming of AlCoCrCuFeNi Multi-Layer High-Entropy Alloy Coatings on AZ91D. *J. Alloys Compd.* **2019**, *772*, 994–1002. [\[CrossRef\]](#)
19. Yang, L.; Li, Z.; Zhang, Y.; Wei, S.; Liu, F. Al-TiC in Situ Composite Coating Fabricated by Low Power Pulsed Laser Cladding on AZ91D Magnesium Alloy. *Appl. Surf. Sci.* **2018**, *435*, 1187–1198. [\[CrossRef\]](#)
20. Guo, Y.; Zhang, Y.; Li, Z.; Wei, S.; Zhang, T.; Yang, L.; Liu, S. Microstructure and Properties of In-Situ Synthesized ZrC-Al<sub>3</sub>Zr Reinforced Composite Coating on AZ91D Magnesium Alloy by Laser Cladding. *Surf. Coatings Technol.* **2018**, *334*, 471–478. [\[CrossRef\]](#)
21. Su, Y.; Yue, T. Microstructures of the Bonding Area in Laser Cladded Zr-Based Amorphous Alloy Coating on Magnesium. *Mater. Today Commun.* **2020**, *25*, 101715. [\[CrossRef\]](#)
22. Lin, P.; Zhang, Z.; Ren, L. The Mechanical Properties and Microstructures of AZ91D Magnesium Alloy Processed by Selective Laser Cladding with Al Powder. *Opt. Laser Technol.* **2014**, *60*, 61–68. [\[CrossRef\]](#)
23. Dziadoń, A.; Mola, R.; Błaż, L. The Microstructure of the Surface Layer of Magnesium Laser Alloyed with Aluminum and Silicon. *Mater. Charact.* **2016**, *118*, 505–513. [\[CrossRef\]](#)
24. Zhang, X.; Zhang, K.; Zou, J. Microstructures and Properties in Surface Layers of Mg-6Zn-1Ca Magnesium Alloy Laser-Clad with Al-Si Powders. *Trans. Nonferrous Met. Soc. China* **2018**, *28*, 96–102. [\[CrossRef\]](#)
25. Wang, Y.; Li, Z.; Zhang, Y.; Wei, S.; Pei, X.; Yang, L. Cold Arc Cladding of Aluminum Coatings on AZ61 Magnesium Alloy: A Comparative Study. *Surf. Coatings Technol.* **2019**, *375*, 442–457. [\[CrossRef\]](#)
26. Zhang, M.; Wang, X.H.; Qu, K.L.; Liu, S.S. Effect of Rare Earth Oxide on Microstructure and High Temperature Oxidation Properties of Laser Cladding Coatings on 5CrNiMo Die Steel Substrate. *Opt. Laser Technol.* **2019**, *119*, 105597. [\[CrossRef\]](#)
27. Zhu, R.; Li, Z.; Li, X.; Sun, Q. Microstructure and Properties of the Low-Power-Laser Clad Coatings on Magnesium Alloy with Different Amount of Rare Earth Addition. *Appl. Surf. Sci.* **2015**, *353*, 405–413. [\[CrossRef\]](#)
28. Quazi, M.M.; Fazal, M.A.; Haseeb, A.S.M.A.; Yusof, F.; Masjuki, H.H.; Arslan, A. Effect of Rare Earth Elements and Their Oxides on Tribo-Mechanical Performance of Laser Claddings: A Review. *J. Rare Earths* **2016**, *34*, 549–564. [\[CrossRef\]](#)
29. Liu, X.; Sui, Y.; Li, J.; Li, Y.; Sun, X.; Liu, C. Laser Metal Deposited Steel Alloys with Uniform Microstructures and Improved Properties Prepared by Addition of Small Amounts of Dispersed Y<sub>2</sub>O<sub>3</sub> Nanoparticles. *Mater. Sci. Eng. A* **2021**, *806*, 140827. [\[CrossRef\]](#)
30. Weng, F.; Yu, H.; Chen, C.; Liu, J.; Zhao, L. Microstructures and Properties of TiN Reinforced Co-Based Composite Coatings Modified with Y<sub>2</sub>O<sub>3</sub> by Laser Cladding on Ti-6Al-4V Alloy. *J. Alloys Compd.* **2015**, *650*, 178–184. [\[CrossRef\]](#)
31. Li, Y.; Xie, F.; Wu, X.; Li, X. Effects of Y<sub>2</sub>O<sub>3</sub> on the Microstructures and Wear Resistance of Si-Al-Y Co-Deposition Coatings Prepared on Ti-Al Alloy by Pack Cementation Technique. *Appl. Surf. Sci.* **2013**, *287*, 30–36. [\[CrossRef\]](#)
32. Yang, L.; Li, Z.; Zhang, Y.; Wei, S.; Wang, Y.; Kang, Y. In-Situ TiC-Al<sub>3</sub>Ti Reinforced Al-Mg Composites with Y<sub>2</sub>O<sub>3</sub> Addition Formed by Laser Cladding on AZ91D. *Surf. Coatings Technol.* **2020**, *383*, 125249. [\[CrossRef\]](#)
33. Yang, Z.; Hao, H.; Gao, Q.; Cao, Y.; Han, R.; Qi, H. Strengthening Mechanism and High-Temperature Properties of H13 + WC/Y<sub>2</sub>O<sub>3</sub> Laser-Cladding Coatings. *Surf. Coatings Technol.* **2021**, *405*, 126544. [\[CrossRef\]](#)

**Disclaimer/Publisher's Note:** The statements, opinions and data contained in all publications are solely those of the individual author(s) and contributor(s) and not of MDPI and/or the editor(s). MDPI and/or the editor(s) disclaim responsibility for any injury to people or property resulting from any ideas, methods, instructions or products referred to in the content.